Skin Friction Extracted from Surface Pressure in Incident Shock-Wave/Boundary-Layer Interaction

Tianshu Liu1[1], David M. Salazar[2]

Western Michigan University, Kalamazoo, MI 49008, USA

Jim Crafton[3], Nickolay Rogoshchenkov[4], Colleen Ryan[5]

Innovative Scientific Solutions, Inc.

7610 McEwen Rd, Dayton, OH 45459

Mark R. Woike[6], David O. Davis[7]

NASA Glenn Research Center, Cleveland, Ohio, 44135

(Final version submitted to AIAA Journal for consideration of publication as a regular paper)

(03/30/2021)

1. The corresponding author, Professor, Department of Mechanical and Aerospace Engineering, Associate Fellow AIAA, tianshu.liu@wmich.edu
2: Research Assistant, Department of Mechanical and Aerospace Engineering
3. Principal Research Engineer, Innovative Scientific Solutions, Inc.
4. Research Engineer, Innovative Scientific Solutions, Inc.
5. Research Engineer, Innovative Scientific Solutions, Inc.
6. Research Engineer, Optics and Photonics Branch
7. Aerospace Engineer, Inlets and Nozzles Branch

Abstract

High-resolution skin friction fields are extracted from pressure sensitive paint (PSP) data obtained in shock-wave/boundary-layer interaction (SWBLI). The method of extracting skin friction from surface pressure is described, including the fundamental relation between skin friction and surface pressure, variational method, error analysis and approximate iterative method. The proposed method is based on a coupling relation between skin friction and surface pressure, where the boundary enstrophy flux (BEF) is suitably modeled or approximated. This method is applied to unsteady PSP data obtained in incident SWBLIs at Mach 2.5 for different Reynolds numbers, revealing the skin friction structures of the flows particularly the separation bubble induced by the incident shock wave. The extracted results are in good agreement with the data obtained by the surface stress sensitive film (S3F).

Nomenclature

A, B	Stern-Volmer coefficients
f_Ω	source term defined in Eq. (2), boundary enstrophy flux
G	source term $G = -\mu f_\Omega$
I	luminescent intensity (radiance)
I_{ref}	luminescent intensity at reference condition (radiance)
$\boldsymbol{K}$	surface curvature tensor
$\boldsymbol{n}$	unit normal vector
p	pressure (N-m^{-2})
Re_D	Reynolds number based on test section diameter

t	time (s)
T	temperature (K)
x_1, x_2	surface or image coordinates (m or pixel)

Greeks:

α	Lagrange multiplier
δp	surface pressure variation (Pa)
μ	viscosity (Pa-s)
ρ	air density (kg-m^{-3})
$\boldsymbol{\tau}$	skin friction vector (N-m^{-2})
$\boldsymbol{\omega}$	vorticity (s^{-1})
Ω	enstrophy (s^{-2})

Abbreviations

BEF	boundary enstrophy flux
CFD	computational fluid dynamics
ISSI	Innovative Scientific Solutions Inc.
LED	light-emitting diode
PSP	pressure sensitive paint
S3F	surface-stress-sensitive film
SWBLI	shock-wave/boundary-layer interaction

I. Introduction

Shock-wave/boundary-layer interactions (SWBLIs) are physical phenomena that often occur in high-speed flows over flight vehicles. The flow structures induced by SWLBI are complex, which significantly affect the aerodynamic characteristics of a flight vehicle. Therefore, deep understanding of SWBLI is of fundamental importance in the design of key systems of high-speed flight vehicles, including wings, control surfaces, bodies, and inlets. Typical SWBLIs include shock impingement to boundary layers (BLs), supersonic flows over compression and divergent ramps, interaction of BLs with shocks generated by vertical fins, and normal shocks on transonic wings. Extensive experimental and computational investigations of SWBLIs have been made to understand the complex flow structures associated with SWBLIs particularly separations induced by SWBLIs [1-7]. SWBLI poses a challenging problem of aerodynamics involving compressibility, turbulence, heat transfer and viscous–inviscid interaction. Computational fluid dynamics (CFD) methods have been used to calculate the flow properties in SWBLI regions, including Reynolds-averaged Navier–Stokes solver, direct numerical simulation, and large-eddy simulation [1, 2]. The numerical results are in acceptable agreement with experimental data in velocity fields and pressure distributions, but significant deviations in skin friction and heat transfer data are found in cases of strong SWBLIs. Therefore, to validate CFD methods, global measurements of surface pressure, skin friction and heat flux are particularly valuable.

A data set of surface pressure in SWBLIs has been established mainly based on measurements using conventional pressure taps distributed in the region of interest, Schlieren method and surface oil visualization, revealing some intriguing aspects of complex flow structures of SWBLIs [8-12]. In contrast, conventional skin friction measuring techniques such as Preston tube, Stanton tube and floating element balance are difficult to use for SWBLIs. Although surface hot-wire and hot-film

sensors were used [13], existing data of skin friction in SWBLIs have been obtained mainly using interferometric oil-film skin friction meter, providing more direct understanding into near-wall flow structures [14-17]. Interferometric oil-film skin friction meter is a semi-direct method to determine absolute values of skin friction at distributed locations in incident SWBLI [16]. To observe skin friction topology in SWBLIs, surface flow visualizations have been conducted by using oil mixed with particles on a surface, and from streaky oil patterns topological structures are conjectured [1-3]. However, some subtle features in complex flows particularly attachment lines and saddles could not be objectively identified using this approach.

Global skin friction diagnostics are critical in experimental studies of SWBLIs. Several global techniques were developed based on relationships between shear-induced deformation of special material structures and measurable quantities, including shear-sensitive liquid crystals [18, 19], surface-stress-sensitive film (S3F) [20] and micro-pillar arrays [21, 22]. Recently, global skin friction diagnostics were developed based on conventional surface flow visualizations including surface oil film, heat transfer, mass transfer, and pressure visualizations [23, 24]. Skin friction is extracted from the measured quantities as an inverse problem when the relations between skin friction and measured quantities are given. These techniques have been used to extract high-resolution skin friction fields in various flows [25-36]. Surface flow visualizations using luminescent oil, pressure and temperature sensitive paints (PSP and TSP) and sublimation coatings have been commonly used in experiments of SWBLIs. It is natural to apply these global techniques to SWBLIs.

The objective of this work is to develop a method of extracting skin friction from surface pressure and determine skin friction fields based on unsteady PSP measurements. First, a coupling relation between skin friction and surface pressure is discussed, where a scalar quantity linking them

contains the boundary enstrophy flux (BEF), the curvature term, and the dilation rate term. This relation is derived from the Navier-Stokes equations for viscous flows. Since this relation enjoys the same mathematical form of the optical flow equation, an inverse problem can be solved using the variational method for extraction of skin friction from measurable surface pressure when the BEF field is given. Next, an approximate method is proposed when the BEF is not exactly known a priori, where a surface pressure variation is applied to a base flow and a skin friction field is determined by an iterative scheme. An error analysis is given to identify the elemental errors and evaluate their contributions to the total skin friction error. Further, the proposed method is applied to unsteady PSP data obtained in incident SWBLIs at Mach 2.5 for different Reynolds numbers in the 17-cm Axisymmetric Wind Tunnel at NASA Glenn Research Center [37, 38]. The extracted skin friction fields from PSP data reveal the detailed structures of the separation bubble induced by the incident shock wave. The results are compared with the data obtained by the surface stress sensitive film (S3F). The experimental setup for PSP and S3F measurements is described in Appendix A, and the measurement uncertainty is discussed in Appendix B.

II. Extraction of Skin Friction from Surface Pressure

A. Basic Relation

Although skin friction and surface pressure are conventionally treated as two independent quantities, there is an explicit coupling relationship between skin friction and surface pressure in viscous flows [34-36]. From a theoretical perspective, the coupling structures of skin friction and surface pressure reveal coherent near-wall structures in complex flows since near-wall flow structures can be completely reconstructed by skin friction and surface pressure [36, 39]. On the other hand, from a standpoint of measurement, the coupling relationship between skin friction and

surface pressure can be used to extract high-resolution skin friction fields as an inverse problem from PSP measurements.

The intrinsic relation between the skin friction vector $\boldsymbol{\tau}$ and the surface pressure p is derived from the Navier-Stokes equations with the no-slip boundary condition in a general surface coordinate system [34, 36]. This on-wall relation is written in a vector form, i.e.,

$$\boldsymbol{\tau} \cdot \nabla p = \mu f_{\Omega}, \tag{1}$$

where f_{Ω} acts as a virtual source term, which is expressed as

$$f_{\Omega} = \mu \left[\frac{\partial \Omega}{\partial n} \right]_{\partial B} - \mu \boldsymbol{\omega}_{\partial B} \cdot \boldsymbol{K} \cdot \boldsymbol{\omega}_{\partial B} + \mu_{\theta} \left(\boldsymbol{\omega}_{\partial B} \times \boldsymbol{n} \right) \cdot \nabla_{\partial B} \theta_{\partial B} \tag{2}$$

where $\Omega = |\boldsymbol{\omega}|^2 / 2$ is the enstrophy, $\partial / \partial n$ is the derivative along the normal direction, $\boldsymbol{\omega} = \nabla \times \boldsymbol{u}$ is the vorticity, $\boldsymbol{K}$ is the surface curvature tensor, $\theta = \nabla \cdot \boldsymbol{u}$ is the dilation rate, μ is the dynamic viscosity, μ_{θ} is the longitudinal viscosity, and $\boldsymbol{n}$ is the unit normal vector of the surface. The subscript ∂B in the variables and operators in Eqs. (1) and (2) denotes the quantities on the surface.

Eq. (1) represents a formal balance between the surface pressure gradient ∇p projected on the skin friction vector $\boldsymbol{\tau}$ and the scalar quantity f_{Ω} that is originated from the diffusion term in the NS equations. In Eq. (2), the first term $\mu \left[\partial \Omega / \partial n \right]_{\partial B}$ is the boundary enstrophy flux (BEF) and the second term is interpreted as the curvature-induced contribution. The term $\boldsymbol{\omega}_{\partial B} \cdot \boldsymbol{K} \cdot \boldsymbol{\omega}_{\partial B}$ in Eq. (2) is formally interpreted as the interaction between the surface curvature and the vorticity on a surface. The quadratic form $\boldsymbol{\omega}_{\partial B} \cdot \boldsymbol{K} \cdot \boldsymbol{\omega}_{\partial B}$ can be transformed into the standard form $\boldsymbol{\omega}_{\partial B} \cdot \boldsymbol{K} \cdot \boldsymbol{\omega}_{\partial B} = \kappa_1 \omega_1^2 + \kappa_2 \omega_2^2$ with the two principal curvatures κ_1 and κ_2, where $\omega_1 = \boldsymbol{\omega}_{\partial B} \cdot \boldsymbol{e}_1$ and

$\omega_2=\boldsymbol{\omega}_{\partial B}\cdot\boldsymbol{e}_2$ are the vorticity components on the principal directions $\boldsymbol{e}_1$ and $\boldsymbol{e}_2$. For a concave surface with $\kappa_1\le 0$ and $\kappa_2<0$ (such as concave ellipsoid and cylinder), $\boldsymbol{\omega}_{\partial B}\cdot\boldsymbol{K}\cdot\boldsymbol{\omega}_{\partial B}<0$. For a convex surface with $\kappa_1\ge 0$ and $\kappa_2>0$ (such as convex ellipsoid and cylinder), $\boldsymbol{\omega}_{\partial B}\cdot\boldsymbol{K}\cdot\boldsymbol{\omega}_{\partial B}>0$. For a hyperboloid surface with $\kappa_1>0$ and $\kappa_2<0$, the sign of $\boldsymbol{\omega}_{\partial B}\cdot\boldsymbol{K}\cdot\boldsymbol{\omega}_{\partial B}$ is undetermined. The ratio between the magnitudes of the second and first terms (the curvature and BEF terms) in Eq. (2) is proportional to δ_c / R_s, where δ_c is the viscous diffusion length scale and R_s is defined as the mean curvature radius of the surface. When the Reynolds number is sufficiently large such that $\delta_c / R_s << 1$, the second term in Eq. (2) could be neglected. In this case, f_Ω is dominated by the BEF. The third term is interpreted as the contribution induced by the temporal-spatial change of the fluid density on the surface.

B. Variational Solution

In this paper, a key problem is how to extract a $\boldsymbol{\tau}$-field from a p-field by solving Eq. (1) for a given f_Ω-field, which is similar to the optical flow problem [40, 41]. The variational formulation is proposed for this inverse problem. We consider the following functional based on the L2 norm $\|\bullet\|_2$ on a domain D

$$J(\boldsymbol{\tau})=\| G+\boldsymbol{\tau}\cdot\nabla p\|_2+\alpha\left\| |\nabla\tau_1|^2+|\nabla\tau_1|^2\right\|_2, \tag{3}$$

where α is a Lagrange multiplier, $G=-\mu f_\Omega$ is a source term, $\boldsymbol{\tau}=(\tau_1,\tau_2)$ is the skin friction vector, $\nabla=\partial/\partial x_i$ ($i=1,2$) is the gradient operator on a surface, and x_i are the surface coordinates. The first term in $J(\boldsymbol{\tau})$ is the equation term. The second term in $J(\boldsymbol{\tau})$ is a

regularization constraint assuming that a τ-field is sufficiently continuous and smooth. Minimizing $J(\tau)$ leads to an Euler-Lagrange equation is obtained, i.e.,

$$(G + \tau \cdot \nabla p)\nabla p - \alpha \nabla^2 \tau = 0, \tag{4}$$

where $\nabla^2 = \partial^2 / \partial x_i \partial x_i$ $(i = 1,2)$ is the Laplace operator on a surface. Given a p-field and a f_Ω-field, Eq. (4) can be solved numerically for a τ-field with the Neumann condition $\partial \tau / \partial n = 0$ on the domain boundary ∂D. The standard finite difference method is used to solve Eq. (4), and the numerical algorithm is essentially the same as that for the optical flow problem in computer vision [38, 39]. In the orthographic projection, the flat surface coordinates are proportional to the image coordinates, and thus x_i are the image coordinates in the present computations. Therefore, for convenience, computations to solve Eq. (4) are directly carried out in the image plane.

C. Approximate Method

Eq. (1) is exactly valid in relating the surface pressure gradient to skin friction. The limitation in applying this equation to recover skin friction is determining the BEF that is defined as the f_Ω term in Eq. (2). In theoretical cases where the BEF is known, a variational solution for this inverse problem is feasible [34]. Unfortunately, for complex flows, the BEF is a difficult quantity to measure experimentally or determine theoretically. Since a f_Ω-field is generally unknown, the solution of Eq. (4) for a τ-field in complex flows cannot be readily obtained for a given p-field only. This problem is considered as a closure problem in which modeling of f_Ω is required. A successive approximation is proposed to obtain a τ-field induced by a surface-pressure variation imposed on a base flow [35]. Figure 1 shows a flow chart of the iterative approximate method. First, in the zeroth-order approximation, a known base flow is considered,

which satisfies $\boldsymbol{\tau}^{(0)} \cdot \nabla p^{(0)} = \mu f_{\Omega}^{(0)}$, where '0' denotes the base flow From a standpoint of application, a base flow could be a relatively simple known steady attached flow such as boundary layer.

Consider a physical situation in which a surface-pressure variation is suddenly imposed on the base flow through a certain external process such as an impinging shock wave. In this case, a composite surface-pressure field (or a perturbed surface-pressure field) on a surface is given by

$$p_c = p^{(0)} + \Delta p, \tag{5}$$

where Δp is a surface-pressure variation. In the first-order approximation, the base-flow BEF $f_{\Omega}^{(0)}$ is not affected in a short time. The underlying assumption is that the process of establishing a Δp-field is much faster than its effect on a f_{Ω}-field. Since pressure is a result of molecules collisions in an equilibrium state, the characteristic timescale of establishing a Δp-field is $t_p \sim l / a_s$, where l is a length scale of a body and a_s is the speed of sound in fluid. In contrast, the physical mechanism of building a f_{Ω}-field is the viscous diffusion, which has a characteristic timescale $t_{\Omega} \sim \delta^2 / \nu$, where δ is a viscous diffusion distance. The characteristic timescales of establishing the Δp-field and f_{Ω}-field are denoted by t_p and t_{Ω}, respectively. An estimate is $t_p / t_{\Omega} \sim M_{ref} / Re_l^{1-2/n}$ [35], where M_{ref} is the local Mach number based on the near-wall velocity scale, and Re_l is the Reynolds number based on a body length scale l and n is an empirical exponent ($n \geq 2$). Therefore, since $t_p / t_{\Omega} << 1$ for $M_{ref} << 1$ near the wall, the underlying approximation is plausible in a short time.

Therefore, the first-order $\boldsymbol{\tau}$-field denoted by $\boldsymbol{\tau}^{(1)}$ can be described by the first-order approximate equation

$$\boldsymbol{\tau}^{(1)} \cdot \nabla p_c = \mu f_\Omega^{(0)}, \tag{6}$$

where $f_\Omega^{(0)}$ is the base-flow BEF. Therefore, a $\boldsymbol{\tau}^{(1)}$-field can be obtained by solving the Euler-Lagrange equation, Eq. (4), with $G = G^{(0)} = -\mu f_\Omega^{(0)}$ that is known for the base flow. A heuristic iteration scheme is $G^{(k)} = -\boldsymbol{\tau}^{(k)} \cdot \nabla p_c$ ($k = 1,2,\cdots$) for iterative improvement in successive higher-order approximations, and accordingly the BEF is given iteratively by $f_\Omega^{(k)} = -\mu^{-1} G^{(k)}$.

Essentially, the approximate method provides a practical alternative where the BEF of a known base flow is used in computation. Thus, a solution obtained by the approximate method gives a skin friction field induced by a surface pressure variation based on the base flow. This approach is applicable to the cases where the skin friction topology is dominated by the pressure gradient. Particularly, SWBLI is such a case where an incoming boundary layer is used as the base flow and a PSP-measured surface pressure variation generated by a shock provides the surface pressure gradient required for computation.

D. Base Flow

A boundary layer could be selected as a base flow, where $\boldsymbol{\tau}^{(0)}$, $p^{(0)}$ and $f_\Omega^{(0)}$ are expressed as the power-law functions of the surface coordinate such that $\boldsymbol{\tau}^{(0)} \cdot \nabla p^{(0)} = \mu f_\Omega^{(0)}$ is satisfied. The base-flow surface pressure and its gradient are given by

$$p^{(0)} = c_0 + \left(c_1 / 2m\right)\left(x - x_0\right)^{2m}, \quad \partial p^{(0)} / \partial x = c_1 \left(x - x_0\right)^{2m-1}, \tag{7}$$

where c_0 and c_1 are proportional coefficients, x_0 is the virtual origin of the boundary layer, and m is a power-law exponent. Accordingly, skin friction and the BEF are given in a form of a power-law relation, i.e.,

$$\tau^{(0)} = c_2 \left(x - x_0 \right)^{(3m-1)/2}, \quad f_\Omega^{(0)} = c_3 \left(x - x_0 \right)^{(7m-3)/2}, \tag{8}$$

where c_2 and c_3 are proportional coefficients. The flow with the power-law distributions of surface pressure, skin friction and BEF serves as a local approximation in many applications. The parameters m and x_0 can be determined by fitting surface pressure data obtained before a surface pressure variation is imposed, as shown in Section III.

A theoretical example is the Falkner-Skan flow (the wedge flow) where the external velocity is $U(x) = a x^m$. The boundary-layer velocity profile is given by $u(x,y)/U(x) = f(\eta)$, where $f(\eta)$ is the similarity function with the similarity variable η, where a is a positive constant and the wedge angle is given by $\pi\beta$ with $\beta = 2m/(m+1)$ [42, 43]. The proportional coefficients are $c_1 = -\rho a^2 m$, $c_2 = \sqrt{(m+1)/2}\,\rho \nu^{1/2} a^{3/2} f''(0)$, and $c_3 = -\mu\beta \left[a(m+1)/2\nu \right]^{3/2} a^2 f''(0)$, where ν is the kinematic viscosity. The value of the second derivative f'' at the wall is approximately expressed as the piecewise functions $f''(0) = 0.749\, m^{0.5049} + 0.4696$ for $0 \le m \le 1$ and $f''(0) = 1.696\, m + 0.4741$ for $-0.06 \le m \le 0.2$ based on its tabulated numerical data [43].

E. Error Analysis

Error Propagation and Constraints

From a computational standpoint, a sensitivity analysis is given, where the sensitivity of skin friction calculation to the elemental errors is evaluated and the selection of the relevant parameters particularly the Lagrange multiplier is discussed. The decompositions $p = p_0 + \delta p$, $G = G_0 + \delta G$ and $\boldsymbol{\tau} = \boldsymbol{\tau}_0 + \delta\boldsymbol{\tau}$ are introduced, where δp, δG and $\delta\boldsymbol{\tau}$ are errors, and p_0, G_0

and $\boldsymbol{\tau}_0$ are the non-perturbed fields that exactly satisfy Eq. (4). Substituting the above decompositions into Eq. (4) and neglecting the higher-order small terms, we have an error propagation equation, i.e.,

$$(\delta\boldsymbol{\tau}\cdot\nabla p_0)\nabla p_0 - \alpha\nabla^2\delta\boldsymbol{\tau} = -(\delta G + \boldsymbol{\tau}_0\cdot\nabla\delta p)\nabla p_0\,, \tag{9}$$

where δG directly contributes to $\delta\boldsymbol{\tau}$ while δp contributes to $\delta\boldsymbol{\tau}$ through a gradient operator projected on the skin friction vector.

To simplify the analysis, in a local region considered, ∇p_0 is a constant vector in a local linear approximation, and the unit normal vector to an iso-pressure line $p_0 = const.$ is $\boldsymbol{N}_T = \nabla p_0 / \|\nabla p_0\|$, where $\|\nabla p_0\|$ is the magnitude of ∇p_0. The skin friction error projected on $\boldsymbol{N}_T$ is defined as $(\delta\boldsymbol{\tau})_N = \delta\boldsymbol{\tau}\cdot\boldsymbol{N}_T$. Normalization of Eq. (9) yields a formal estimate of the relative error, i.e..

$$\frac{(\delta\boldsymbol{\tau})_N}{\|\boldsymbol{\tau}_0\|} = -\frac{\delta G}{\|\nabla p_0\|\|\boldsymbol{\tau}_0\|} - \left(\frac{\boldsymbol{\tau}_0}{\|\boldsymbol{\tau}_0\|}\right)\cdot\delta\boldsymbol{N}_T + \frac{\alpha}{\|\nabla p_0\|^2}\nabla^2\left[\frac{(\delta\boldsymbol{\tau})_N}{\|\boldsymbol{\tau}_0\|}\right], \tag{10}$$

where $\|\boldsymbol{\tau}_0\|$ is a characteristic value of skin friction (e.g. the mean value). The first term in the RHS of Eq. (10) is the contribution from the elemental error in measurement of the term *G*. The second term is the contribution from the elemental error in measurement of the surface gradient of the relative intensity. The third term is the contribution from the artificial diffusion of the error $(\delta\boldsymbol{\tau})_N$ associated with the Lagrange multiplier.

The first and third terms in the RHS of Eq. (10) are proportional to $\|\nabla p_0\|^{-1}$ and $\|\nabla p_0\|^{-2}$, respectively. This indicates that the relative error $(\delta\boldsymbol{\tau})_N / \|\boldsymbol{\tau}_0\|$ will be very large when $\|\nabla p_0\|$ approaches zero, which imposes an intrinsic limitation on application of this technique in certain

regions where $\|\nabla p_0\|$ is close to zero. The proportional factor in the third term is $\alpha\|\nabla p_0\|^{-2}$. Therefore, the Lagrange multiplier α must be sufficiently small to reduce the error particularly when $\|\nabla p_0\|$ is small. On the other hand, for an ill-posed problem, a variational solution with a regularization parameter α is affected by the data error (or measurement error), The choice of the regularization parameter α depends on δ, i.e., $\alpha = \alpha(\delta)$, where a positive numerical value δ is a bound of the data error. The resulting error of the solution decreases in $\delta/\sqrt{\alpha}$ as $\delta \to 0$ [44, 45]. To ensure the convergence of the solution, the condition is $\delta^2/\alpha(\delta) \to 0$, indicating that the data error must be reduced as α decreases. In regions where $\|\nabla p_0\|$ is small, α should be small according to Eq. (10), and thus the data error bound δ must be tightly controlled for the acceptable accuracy of the solution. Otherwise, the error of the regularized solution could be large in these regions.

PSP Measurement Limit

From a standpoint of measurements, the accurate determination of $\|\nabla p_0\|$ is limited by the resolvable pressure limit of PSP. For a digital camera, the minimum pressure difference that PSP can measure from a single frame of image is given by [46]

$$\frac{(\Delta p)_{min}}{p} = \frac{1}{\sqrt{(n_{pe\,ref})_{max}}}\left[1 + \frac{A(T)}{B(T)}\frac{p_{ref}}{p}\right]\left[1 + A(T) + B(T)\frac{p}{p_{ref}}\right]^{1/2}, \tag{11}$$

where $(n_{pe\,ref})_{max}$ is the full-well capacity of a camera in a reference condition, $A(T)$ and $B(T)$ are the Stern-Volmer coefficients in the calibration curve of PSP, and p and p_{ref} are the wind-on and wind-off pressures, respectively. When N images are averaged, the limiting pressure difference

given by Eq. (11) is further reduced by a factor $N^{1/2}$. Eq. (11) provides an estimate for the noise-equivalent pressure resolution for a camera. Structures with a surface pressure variation smaller than that given by Eq. (11) cannot be extracted by the proposed method from PSP images.

Effect of Turbulence

From a physical standpoint, certain flow mechanisms that lead to a significant change in skin friction do not significantly change surface pressure. For example, when the boundary-layer transition occurs, turbulence leads to a significant increase in skin friction while a surface pressure distribution is not changed much. In this case, a skin friction field affected by turbulence cannot be extracted based on a surface pressure field alone without modeling the effect of turbulence. To illustrate this, we consider the Reynolds decompositions $p = \langle p \rangle + p'$, $f_\Omega = \langle f_\Omega \rangle + f'_\Omega$ and $\boldsymbol{\tau} = \langle \boldsymbol{\tau} \rangle + \boldsymbol{\tau}'$, where $\langle\ \rangle$ denotes the time-averaging operator and the prime denotes fluctuation. Therefore, we have the time-averaged relation $\langle \boldsymbol{\tau} \rangle \cdot \nabla \langle p \rangle = \mu \langle f_\Omega \rangle - \langle \boldsymbol{\tau}' \cdot \nabla p' \rangle$. Clearly, to take the effect of turbulence into account, the correlation term $\langle \boldsymbol{\tau}' \cdot \nabla p' \rangle$ should be modeled as an additional contribution to the time-averaged BEF. Neglecting this term could lead to an error.

III. Incident Shock-Wave/Boundary-Layer Interaction

A. Time-Averaged Surface Pressure and Skin Friction Fields

Unsteady pressure and surface shear stress (skin friction) measurements in incident SWBLIs were conducted by Woike et al. [37] in the NASA Glenn Research Center 17-cm Axisymmetric Wind Tunnel (the 17-cm Axi-SWT) (see Appendix A for details). The results obtained by using fast PSP and surface stress sensitive films (S3F) [20] provide a good set of data to examine the

proposed method of extracting skin friction from surface pressure. The experimental conditions of the test cases in this work are listed in Table 1. A shock generated by a 13.5^o cylindrical cone impinges on the wall and interacts with the floor boundary layer at different total pressures and Reynolds numbers (Re_D) based on the test section diameter. Figure 2 shows the SWBLI region of interest in the Mach 2.5 Axisymmetric test section [37, 38], where the origin of the *x*-coordinate is set at the location of the maximum surface pressure gradient in the surface pressure rise induced by the impinging shock. Unsteady PSP measurements were made using Innovative Scientific Solutions Inc. (ISSI) Turbo PSP with 2 kHz time response, and images were acquired at 4 kHz using the Photron SA-Z high-speed camera. Surface pressure fields are converted from PSP images using the calibration relation, where PSP image in the wind-off case (Case 3464) is used as the reference image.

Figure 3 shows the time-averaged surface pressure fields normalized by the atmospheric pressure ($p_{stm} = 1\,atm$) at Mach 2.5, where the Reynolds numbers (Re_D) based on the test section diameter (17 cm) are 5, 4, 3, 2 and 1.5 million from the top to bottom, respectively. These fields are obtained by averaging sequences of 2000 fields. The coordinates are normalized by the boundary-layer thickness δ = 13.1 mm measured at about 5 mm before the shock impingement [38]. The corresponding span-averaged profiles of surface pressure in the *x*-coordinate are shown in Fig. 4. Here, the origin of the *x*-coordinate is set at the location where the maximum surface pressure gradient is attained at Re_D = 5 million. The rise of surface pressure induced by the shock increases with Re_D. The separation and re-attachment locations are marked in Fig. 4, which are determined as the zero-crossing points in the *x*-component of skin friction (see Figs. 6 and 7). Here, the bubble length L_b is introduced as the distance between a point where surface pressure

starts to rapidly rise and a downstream point where surface pressure starts to level off. An estimate is $L_b / \delta \approx 1$, which is consistent with CFD simulation [47]. It is noted that visible vertical stripes in these images are caused by the fixed-pattern noise of the camera (see Appendix B).

For further comparison, the surface pressure profiles in Fig 4 are re-normalized by the values at the location (x = -65 mm) upstream of the shock, as shown in Fig. 5. The surface pressure data in the incoming boundary layer before the region of incident SWBLI is fitted using the power-law relation

$$p(x) / p(x_{ref}) = 3.65 - (x - x_0)^{2m}, \tag{12}$$

where the virtual origin of the incoming boundary layer is $x_0 = -200\ mm$, the reference location is $x_{ref} = -65\,mm$, and the power-law exponent is $m = 0.1$. This power-law relation will be used as the base-flow surface pressure distribution in the reconstruction of τ-fields. The surface pressure increases rapidly to the peak immediately after a shock and then decays in a downstream region of 100 mm. The ratio between the PSP-measured surface pressures after and before a shock is $p_2 / p_1 \approx 1.6 - 1.75$ in a range of Re_D from 1.5 to 5 million, which is consistent with the value of $p_2 / p_1 \approx 1.7$ given by Davis [38] based on the pressure tap measurement.

The τ-fields are extracted from the corresponding surface pressure fields using the approximate method described in Section II. The incoming boundary layer is used as the base flow with the power–law distributions of surface pressure and BEF where the exponent is $m = 0.1$. The Lagrange multiplier is set at $\alpha = 10^{-5}$ in solving the Euler-Lagrange equation Eq. (4) and four iterations are used for successive approximations. Since the proportional coefficient in the BEF field is not determined, relative τ-fields are extracted, and therefore normalized τ-fields are presented. Figure 6 shows the time-averaged fields of surface pressure normalized by its

maximum value, τ-vectors and τ-lines at Mach 2.5 for Re_D = 5 million in Case 3466. The results are nominally two-dimensional since the width of the region is much smaller than the radius of the circular test section. The azimuthal effect on these results cannot be seen in this narrow region. There are 230×420 vectors extracted in the regions of interest in Fig. 6, and the spatial resolution of the data is one vector per pixel. One pixel corresponds to 16 μm on the surface. The separation bubble induced by incident SWBLI occurs in all the cases. The separation and re-attachment lines are clearly identified in the skin friction topology in Fig. 6. A separation line is identified as a τ-line to which neighboring τ-lines converge, while an attachment line is a τ-line from which neighboring τ-lines diverge. Figure 7 shows the time-averaged fields of normalized surface pressure by its maximum value, extracted skin friction vectors and lines at Mach 2.5 for Re_D = 4, 3, 2, and 1.5 million. Figure 8 shows the span-averaged profiles of the *x*-component of τ in the *x*-coordinate at Mach 2.5 for different Reynolds numbers. The zero-crossing points in Fig. 8 give the separation and re-attachment locations indicated in Fig. 4. It is observed that as Re_D decreases, the separation bubble slightly moves upstream.

B. Comparison with S3F Data

Measurements with S3F were made in incident SWBLIs generated by the 13.5° shock generator at Mach 2.5 at Re_D = 1.5 and 2 million [37]. Figures 9-12 show comparisons between the results obtained by PSP and S3F in the region near the separation bubble for Re_D = 2 and 1.5 million. The τ-field obtained by S3F has 23×49 vectors in the region, in contrast to 231×476 vectors extracted from PSP data. The spatial resolution of S3F is limited by the thickness of the film and the size of interrogation windows in cross-correlation calculation. The S3F data

presented here were acquired using a film of about 1 mm thickness. Processing was accomplished using the cross-correlation method in interrogation windows of 10×10 pixels (the corresponding spatial scale of about 4 mm^2) and 50% overlap, resulting in a field of 23×49 vectors. For Re_D = 1.5 million, the mean values of skin friction of about 43 and 34 Pa were measured by S3F at an upstream location (x = -75 mm) and the window centerline, respectively. These results are approximately correspond to 39 and 37 Pa given by CFD [37]. As an additional reference, an estimated value of skin friction at the far upstream (x = -555 mm) was 55 Pa, which was inferred by fitting the velocity data to the log-law profile in a turbulent boundary layer [38]. The extrapolated value at x = -75 mm based on the power-law formula of the skin friction coefficient for a turbulent boundary layer on a flat plate is 47 Pa, which is close to 43 Pa given by S3F.

The relative τ-fields obtained by PSP are anchored in in-situ calibration by using the S3F data (52 and 41 Pa for Re_D = 2 and 1.5 million, respectively) at the reference location x = 20 mm marked in Figs. 9-12. The separation bubble is detected by both PSP and S3F. The results obtained by PSP exhibit some 3D features particularly the streamwise streaky structures after re-attachment. The span-averaged profiles of the x-component of τ are shown in Figs. 10 and 12, indicating that the results extracted from PSP are in agreement with the S3F data. Note that in Figs. 10 and 12, S3F data in the upstream and downstream regions were obtained separately from different sets of images.

C. Properties of Fluctuations

PSP image were acquired at 4,000 fps, and thus time sequences of surface pressure and skin friction fields were obtained. The variances of the surface pressure fluctuation $p' = p - \langle p \rangle$ and

skin friction fluctuation $\boldsymbol{\tau}' = \boldsymbol{\tau} - \langle \boldsymbol{\tau} \rangle$ are calculated from sequences of 2500 fields, where $\langle \bullet \rangle$ denotes the time-averaging operator. Figure 13 shows the fields of the variances $\left\langle |\boldsymbol{\tau}'|^2 \right\rangle$ and $\left\langle p'^2 \right\rangle$ normalized by their maximum values at the Mach 2.5 for Re_D = 2 million. The variance $\left\langle |\boldsymbol{\tau}'|^2 \right\rangle$ has peaks near the separation and re-attachment lines of the separation bubble. The variance of $\left\langle p'^2 \right\rangle$ starts to increase across the separation bubble. The energy spectra of the fluctuations $\boldsymbol{\tau}'$ and p' along the streamwise centerline of the measurement region are shown in Fig. 14, where the spectra are normalized by the $max\left[P(\boldsymbol{\tau}'_x) + P(\boldsymbol{\tau}'_y) \right]$ and $max\left[P(p') \right]$, respectively, and P denotes the energy spectrum. It is found in Figs. 14(a) and 14(b) that the fluctuations of the skin friction components are contributed mainly by the low-frequency contents (< 10 Hz), which are concentrated near the separation and re-attachment lines of the separation bubble. The *x*-component of $\boldsymbol{\tau}'$ has the much larger energy than the *y*-component of $\boldsymbol{\tau}'$. As shown in Fig. 14(c), the energy of p' is mainly contributed by the low-frequency contents as well, which increases across the incident SWBLI region. The increase of the energy of p' across the incident SWBLI region is found in large-eddy simulations [47, 48]. As shown Figs. 15 and 16, the fluctuations of skin friction and surface pressure at Re_D = 1.5 million have similar behaviors near the separation bubble.

IV. **Conclusions**

The method of extracting skin friction fields from PSP images is developed based on a coupling relation between skin friction and surface pressure. The variational method is used to solve this inverse problem, and the Euler-Lagrange equation is obtained for extraction of skin

friction from surface pressure. The approximate method gives a skin friction field induced by a surface pressure variation based on the base flow, where the base flow with the power-law forms of the surface pressure and BEF distributions are used. This method is particularly suitable for the flows where the skin friction topology is dominated by the pressure gradient. The error analysis indicates that the Lagrange multiplier plays a critical role in the calculation. The approximate method is applied to PSP images obtained in incident shock-wave/boundary-layer interaction (SWBLI). The high-resolution skin friction fields extracted from time sequences of PSP images at different Reynolds numbers clearly reveal the detailed structures characterized by the separation and re-attachment lines of the separation bubble induced by the incident shock. The separation bubble slightly moves upstream as the Reynolds number decreases. The time-averaged normalized skin friction distributions extracted from PSP images are in agreement with the data obtained by surface shear sensitive film (S3F) at the Reynolds numbers (Re_D) of 2 and 1.5 million. The variance of the skin friction fluctuation has peaks near the separation and re-attachment lines, while the variance of surface pressure fluctuation rapidly increases across the separation bubble. The fluctuations of skin friction and surface pressure are dominated by the low-frequency contents.

Acknowledgements:

This work was supported by the NASA SBIR (NNC14QA53P and 80NSSC19C0414) and the Transformational Tools & Technologies Project of the NASA Transformative Aeronautics Concepts Program.

References:

[1] Babinsky, H. and Harvey, J. K., Shock Wave–Boundary-Layer Interactions, Cambridge University Press, Cambridge, UK, 2011.

[2] Knight, D., Yan, H., Panaras, A. G., and Zheltovodov, A., "Advances in CFD Prediction of Shock Wave Turbulent Boundary Layer Interactions," Prog. Aero. Sci., Vol. 39, No. 2, 2003, pp. 121–184.

[3] Délery, J. and Dussauge, J-P., "Some Physical Aspects of Shock Wave/Boundary Layer Interactions," Shock Waves, Vol 19, No. 2009, pp. 453–468

[4] Dolling, D. S., Fifty Years of Shock-Wave/Boundary-Layer Interaction Research: What Next?, AIAA J., Vol. 39, No. 8, 2001, pp. 1517-1531.

[5] Panaras, A. G., Review of the physics of Swept-Shock/Boundary-Layer Interactions, Prog. Aero. Sci., Vol. 32, 1996, pp. 173-244.

[6] Settles, G. S., and Dolling, D. S., "Swept Shock/Boundary-Layer Interactions—Tutorial and Update," AIAA Paper 90-0375, Jan. 1990.

[7] Settles, G. S., "Recent Skin Friction Technologies for Compressible Flows," AIAA Paper 86-1099, May 1986.

[8] Dolling, D. S. and Rodi, P. E., "Upstream Influence and Separation Scales in Fin-Induced Shock Turbulent Boundary-Layer Interaction," J. Spacecraft and Rockets, Vol. 25, No. 2, 1988, pp. 102-108.

[9] Settles, G. S. and Kimmel, R. L., "Similarity of Quasiconical Shock Wave/Turbuluent Boundary-Layer Interactions," AIAA J., Vol. 24, No. 1, 1986, pp. 47-53.

[10] Settles, G. S. and Bogdonoff, S. M., "Scaling of Two- and Three-Dimensional Shock/Turbulent Boundary-Layer Interactions at Compression Corners," AIAA J., Vol. 20, No. 6, 1982, pp. 782-789.

[11] Lu, F. K., Quasiconical Free Interaction Between a Swept Shock and a Turbulent Boundary Layer, AIAA J., Vol. 31, No. 4, 1993, pp. 686-692.

[12] Reda, D. C. and Murphy, J. D., "Shock-Wave/Turbulent-Boundary- Layer Interactions in Rectangular Channels," AIAA J., Vol. 11, No. 2, 1973, pp. 139, 140; also AIAA Paper 72-715, 1972.

[13] Murthy, V. S. and Rose, W. C., "Wall Shear Stress Measurements in a Shock-Wave/Boundary-Layer Interaction," AIAA J., Vol. 16, No. 7, 1978, pp. 667–672.

[14] Kim, K.-S., Lee, Y., Alvi, F. S., Settles, G. S., and Horstman, C. C., "Skin-Friction Measurements and Computational Comparison of Swept Shock/Boundary-Layer Interactions," AIAA J., Vol. 29, No. 10, 1991, pp. 1643–1650.

[15] Alvi, F. S., and Settles, G. S., "Physical Model of the Swept Shock-Wave/Turbulent Boundary-Layer Interaction Flowfield," AIAA J., Vol. 30, No. 9, 1992, pp. 2252–2258.

[16] Schülein, E., Skin-Friction and Heat Flux Measurements in Shock/Boundary-Layer Interaction Flows, AIAA J.., Vol. 44, No. 8, 2006, pp. 1732-1741.

[17] Naughton, J. W., and Sheplak, M., "Modern Developments in Shear stress Measurements," Prog. Aero. Sci, Vol. 38, No. 6, 2002, pp. 515–570.

[18] Reda, D. C., Wilder, M. C., Farina, D. J., and Zilliac, G. "New Methodology for the Measurement of Surface Shear Stress Vector Distributions," AIAA J., Vol. 35, No. 4, 1997, pp. 608-614.

[19] Reda, D. C. and Wilder, M. C. “Shear-Sensitive Liquid Crystal Coating Method Applied through Transparent Test Surfaces,” AIAA J., Vol. 39, No. 1, 2001, pp. 195-197.

[20] Fonov, S. D., Jones, G., Crafton, J., Fonov, V. and Goss, L. “The Development of Optical Technique for the Measurement of Pressure and Skin Friction,” Meas. Sci. Technol., Vol. 17, 2006, pp. 1261-1268.

[21] Brücker, C., Bauer, D. and Chaves, H..” Dynamic Response of Micro-Pillar Sensors Measuring Fluctuating Wall-Shear-Stress,” Exp Fluids, Vol. 42, 2007, pp. 737–749.

[22] Große, S. and Schröder, W. “Mean Wall-Shear Stress Measurements Using the Micro-Pillar Shear-Stress Sensor,” Meas. Sci. Technol., Vol. 19, 2008, p. 015403.

[23] Liu, T., “Extraction of Skin-Friction Fields from Surface Flow Visualizations as an Inverse Problem,” Meas. Sci. Technol., Vol. 24: 2013, p. 124004.

[24] Liu, T., “Global Skin Friction Measurements and Interpretation,” Prog. Aero. Sci., Vol. 111, Sep., 2019, p. 100584.

[25] Liu, T., Montefort, J., Woodiga, S., Merati, P. and Shen, L. “Global Luminescent Oil Film Skin Friction Meter,” AIAA J., Vol. 46, No. 2, 2008, pp. 476-485.

[26] Liu, T. Woodiga, S. and Ma, T. “Skin Friction Topology in a Region Enclosed by Penetrable Boundary,” Exp Fluids, Vol. 51, 2011, pp. 1549-1562.

[27] Woodiga, S. and Liu, T. “Skin Friction Fields on Delta Wings,” Exp Fluids, Vol. 47, 2009, pp. 897-911.

[28] Husen, N., Liu, T. and Sullivan, J. P. “The Luminescent Oil Film Flow Tagging (LOFFT) Skin Friction Meter Applied to FAITH Hill,” AIAA J., Vol, 56, No. 10,: 2018, pp. 3875-3886.

[29] Zhong, H., Woodiga, S., Wang, P. J., Shang, J., Cui, X., Wang, J. and Liu, T. "Skin Friction Topology of Wing-Body Junction Flows," European J. of Mechanics – B/Fluids, Vol. 53, 2015, pp. 55-67.

[30] Liu, T. and Woodiga, S. "Feasibility of Global Skin Friction Diagnostics Using Temperature Sensitive Paint," Meas. Sci. Technol. Vol. 22, 2011, p. 115402.

[31] Miozzi, 1. M., Capone, A., Di Felice, A., Klein, C. and Liu, T. "Global and Local Skin Friction Diagnostics from TSP Surface Patterns on an Underwater Cylinder in Cross Flow," Physics of Fluids, Vol. 28, No. 12, 2016, pp.: 12410.

[32] Liu, T., Woodiga, S., Gregory, J. and Sullivan, J. P. "Global Skin Friction Diagnostics Based on Surface Mass-Transfer Visualizations," AIAA J., Vol. 52, No. 11, 2014, pp: 2369-2383.

[33] Liu, T., Makhmalbaf, M. H. M., Ramasamy, R. S. V., Kode, S. and Merati, P. "Skin Friction Fields and Surface Dye Patterns on Delta Wings in Water Flows," J. Fluids Engineering, Vol. 137, 2015, p. 071202-1-14.

[34] Liu, T., Misaka, T., Asai, K., Obayashi, S, and Wu, J. Z. "Feasibility of Skin-Friction Diagnostics Based on Surface Pressure Gradient Field," Meas. Sci. Technol., Vol. 27, No. 12, 2016, pp. 125304.

[35] Liu, T., "Skin-Friction and Surface-Pressure Structures in Near-Wall Flows," AIAA J., Vol. 56, No. 10, 2018, pp. 3887-3896.

[36] Chen, T., Liu, T., Wang, L-P and Chen, S. Y. "Relations between Skin Friction and Other Surface Quantities in Viscous Flows," Physics of Fluids, Vol. 31, 2019, p. 107101.

[37] Woike, M. R., Davis, D. O., Clem, M. M. and Crafton, J. "The Investigation of Shock Wave Boundary Layer Interactions Using Fast Pressure Sensitive Paint and Surface Stress Sensitive Film Measurement Techniques," AIAA Paper 2017-3732, 2017.

[38] Davis, D. O., "CFD Validation Experiment of a Mach 2.5 Axisymmetric Shock-Wave/Boundary-Layer Interaction," ASME Paper AJK2015-06342, ASME/JSME/KSME 2015 Joint Fluids Engineering Conference, Seoul, KOREA, July 26-31, 2015 (also NASA TM-2015).

[39] Bewley, T. and Protas, B., "Skin Friction and Pressure: The "Footprints" of Turbulence." Physica D, Vol. 196, No. 1-2, 2004, pp. 28-44.

[40] Horn, B. K. and Schunck, B. G. "Determining Optical Flow," Artificial Intelligence, Vol. 17, No. 1-3, 1981, pp. 185-204.

[41] Liu, T. and Shen, L. "Fluid Flow and Optical Flow," J. Fluid Mech., Vol. 614, 2008, pp. 253-291.

[42] Schlichting, H. "Boundary-Layer Theory (7th Edition)," McGraw-Hill, New York, 1979, Chapters XII and XVI.

[43] Ishak, A., Nazar, R. and Pop, I. "Falkner-Skan Equation for Flow Past a Moving Wedge with Suction or Injection," J. Appl. Math & Computing, Vol. 25, No. 1-2, 2007, pp. 67-83.

[44] Tikhonov, A. N. and Arsenin, V. V. "Solutions of Ill-Posed Problems." Wiley, New York, 1977, Chapter II.

[45] Groetsch, C. W. "Inverse Problems in the Mathematical Sciences," Vieweg Braunschweig, 1993, Chapter 5.

[46] Liu, T. and Sullivan, J. P. "Pressure and Temperature Sensitive Paints," Springer, Berlin, 2005, Chapters 1, 3 and 5.

[47] Pirozzoli, S. and Bernardini, M. "Direct Numerical Simulation Database for Impinging Shock Wave/Turbulent Boundary-Layer Interaction," AIAA J., Vol. 49, No. 6, 2011, pp. 1307-1312.

[48] Hadjadj, A. "Large-Eddy Simulation of Shock/Boundary-Layer Interaction, AIAA J., Vol. 50, No. 12, 2012, pp. 2919-2927.

Appendix A: PSP and S3F Measurements

Woike et al. [37] conducted unsteady pressure and surface skin friction measurements in incident SWBLIs using fast PSP and surface stress sensitive films (S3F) in the NASA Glenn Research Center 17-cm Axisymmetric Wind Tunnel (the 17-cm Axi-SWT). This wind tunnel was specifically designed for two dimensional CFD code validation experiments on shock/boundary layer interactions to minimize the complex 3D separation often occurred in incident SWBLI in a conventional rectangular test section. The detailed descriptions of the configuration and basic flows of the 17-cm Axi-SWT are given by Davis [38]. The tunnel has a round test section operating at Mach 2.5 with a cone-cylinder centerbody. The cone-cylinder centerbody generates a conical shock that impinges on and reflects off the cylindrical test section wall and interacts with the test section's naturally occurring boundary layer. The centerbody with the cone angle of 13.5° was used to generate the conical shocks. Figure A1 shows the cylindrical test section with one of the shock generators installed. The measured boundary-layer thickness at the nozzle exit was approximately 6.1 mm, and the shape factor was about 1.4, indicating a fully turbulent boundary layer exhibiting the log-law velocity profiles. The measured boundary-layer thickness at a location before the shock impingement was approximately 13.1 mm.

Figure A2 shows a schematic of the test section and window with the dimensions. To make optical measurements, optically clear cast acrylic test section windows were designed and fabricated specifically for PSP and S3F, as shown in Fig. A3. The inside surface of these windows were contoured to match the surface of the test section wall. The paints and films were applied to the flow surface side of the window and imaged from the back side looking through the window. Two windows were used for unsteady PSP measurements, one with the 2 kHz response paint (FIB PSP) and the other with the 30 kHz paint (porous PSP). The paints were produced by Innovative

Scientific Solutions Inc. (ISSI). Two of the windows were used for the surface stress sensitive film measurements. The windows were inserted in the window opening in the test section to make the desired optical pressure and surface stress measurements. The axial placement of the cone tip was chosen so that the conical shock generated by the cone impinged at approximately the center of the window location in the test section.

For a typical PSP, the Stern-Volmer relation is [46]

$$\frac{I_{ref}\left(p_{ref},T\right)}{I\left(p,T\right)} = A\left(T\right) + B\left(T\right)\frac{p}{p_{ref}}, \tag{A1}$$

where I is the luminescent intensity pf PSP, p is pressure, T is temperature, I_{ref} and p_{ref} are the luminescent intensity and pressure at reference condition, respectively, and A B are the Stern-Volmer coefficients. Figure A4(a) shows the Stern-Volmer plots of ISSI Turbo PSP (FIB PSP) used in the present measurements, where p_{ref} is one atmospheric pressure. Figure A4(b) shows the normalized reference luminescent intensity $I_{ref}\left(p_{ref},T\right)$ as a function of temperature for ISSI Turbo PSP, where T_{ref} is 298.15 K (25 ^{o}C). It is indicated that the data at different temperatures collapse into a single straight line such that the Stern-Volmer coefficients are independent from temperature. The Stern-Volmer coefficients determined by fitting the data are $B = 0.806$ and $A = 0.178$. Therefore, ISSI Turbo PSP is a special PSP called 'ideal PSP' that is advantageous in correcting the effect of temperature on PSP measurement [46].

PSP images were acquired using a Photron SA-Z high-speed camera and two LED units for illumination (ISSI LM4XX-400). The Photron SA-Z is a fast framing CMOS camera with a spatial resolution of 1024×1024 pixels and 12-bit dynamic range. The camera is capable of acquiring images at up to 20 kHz full frame, and over 100 kHz at reduced resolution. However, in

this experiment, PSP images were acquired at 4 kHz using both the 30 kHz and 2 kHz PSPs. The camera and LED units were set up on the same side external to the test section looking through the backside of the window that had PSP applied to its inner surface. The PSP measurement setup at the Mach 2.5 axisymmetric test section is shown in Fig. A5.

As was the case for PSP measurements, imaging and illumination for the surface-stress-sensitive film (S3F) applied to the inside flow surface were accomplished by looking through the backside of the window. S3F is a direct method to measure surface shear force, which involves mounting a thin film of a flexible elastomer of known thickness and shear modulus onto a surface [20]. Fluorescent markers (particles) are introduced into the film as a means of measuring their displacement under tangential load due to the flow. The surface shear stress is determined using Hooke's law relating shear stress to shear strain. When the film surface undergoes tangential displacement due to the load, the markers will be displaced as the film shears. The stressed film displacement is a function of the applied shear force, the thickness of the film, and its shear modulus. Hence, when the displacement field is determined using the cross-correlation method in PIV, the surface shear stress field can be determined for the given thickness of the film and its shear modulus. In this experiment, four PCO 12-bit CCD cameras were used to image the entire window area. The separate images were analyzed using a cross-correlation technique comparing wind-off to wind-on images and stitched together to yield the two dimensional shear stress maps.

Appendix B: Measurement Uncertainty

Uncertainty of PSP measurement is contributed by some elemental error sources, including camera noise, illumination variation, model motion, temperature effect, and photodegradation [46]. Wind-on and wind-off images are aligned using the image transformation to minimize the error

caused by the motion of the surface. The temperature effect is usually a dominant error source in PSP measurements. However, ISSI Turbo PSP was used as an ideal PSP that has a single calibration relation with the Stern-Volmer coefficients independent from temperature (see Appendix A). Thus, the temperature effect is largely minimized. The effect of photodegradation is neglected since the run time was short. Now, we estimate the camera noise including the photon shot noise, dark current and fixed pattern noise. Figure B1 shows typical dark current image, wind-off image, and wind-on image in Case 3466. The fixed-pattern noise with vertical stripes are observed in these images. From the dark current image, the estimated root-mean-square (RMS) error is about 1.8 counts, including the dark current and fixed-pattern noise. From the wind-off image at a constant pressure, the estimated RMS error is about 11.6 counts, including the photon shot noise, dark current, and fixed-pattern noise. Since the dark current and fixed-pattern noise are subtracted in image processing, the estimated RMS error due to the photon shot noise is about 10 counts. For the wind-off images with the averaged intensity of 1000 counts, the relative uncertainty due to the camera noise in luminescence measurement is about $\sigma(I)/I \sim 1\%$, where $\sigma(I)$ denotes the luminescent intensity. Based on the Stern-Volmer relation Eq. (A1), the relative uncertainty in pressure is $\sigma(p)/p \sim 1\%$ since it is approximately proportional to that in luminescent intensity. Further, in terms of the uncertainty in skin friction, the second term in the RHS of Eq. (10) is about 1%. The first and third terms in Eq. (10) are related to the modeling of the BEF term and the variational method, which are not known a priori.

Table 1: Test Conditions for Shock-Wave/Boundary-Layer Interaction

Test Case	Cone Angle (degree)	Total Pressure (psia)	Total Temperature (R)	Mach Number	Reynolds Number Re_D ($\times 10^6$)
3464	13.50	14.46	530.03	0.0	0.0
3465	13.50	1.80	525.62	0.0	0.0
3466	13.50	43.49	532.10	2.50	5.00
3467	13.50	34.74	531.79	2.50	4.00
3468	13.50	26.04	531.36	2.50	3.00
3469	13.50	17.30	531.14	2.50	2.00
3470	13.50	13.00	531.12	2.50	1.50

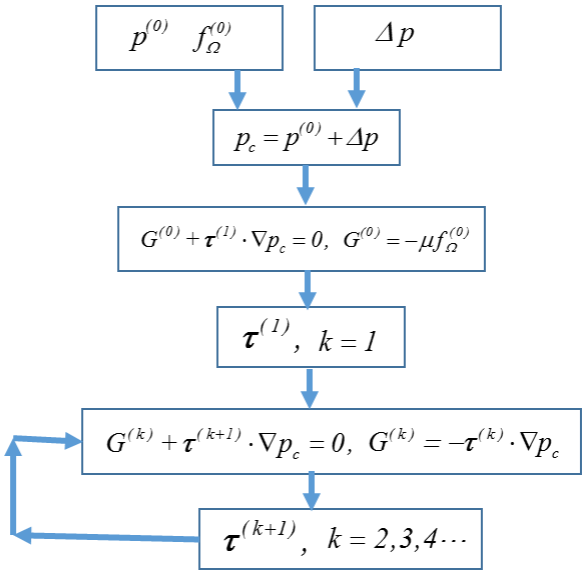

Figure 1. Flow chart of the iterative approximate method.

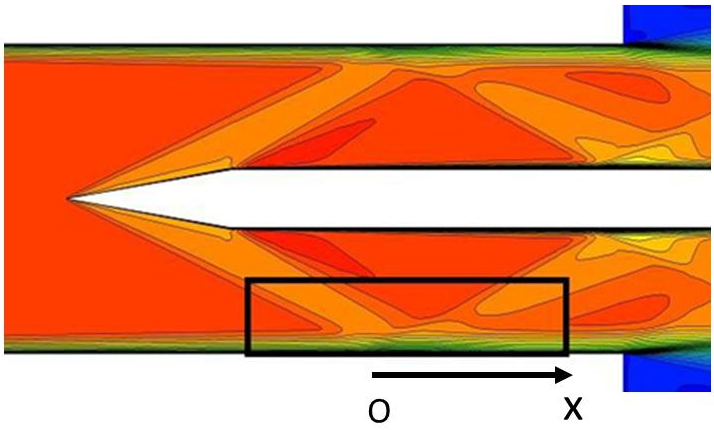

Figure 2. SWBLI region of interest (marked by a rectangle) in the Mach 2.5 Axisymmetric test section [37, 38]. Flow is from left to right.

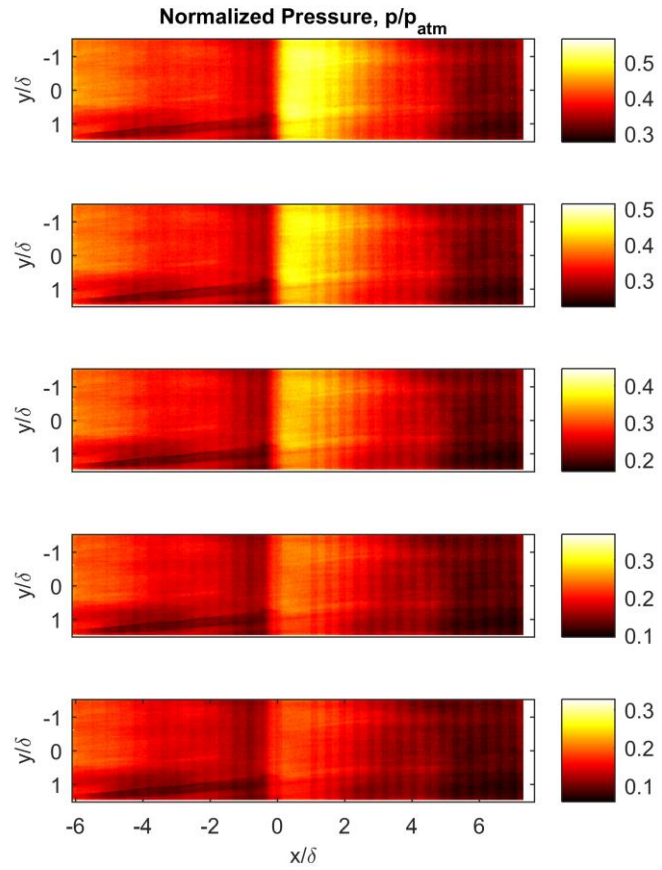

Figure 3. Time-averaged surface pressure fields normalized by one atmospheric pressure at Mach 2.5 in incident SWBLI generated by a 13.5° cylindrical cone. From the top plot to bottom plot, the Reynolds numbers (Re_D) are 5, 4, 3, 2 and 1.5 million, respectively. Flow is from left to right.

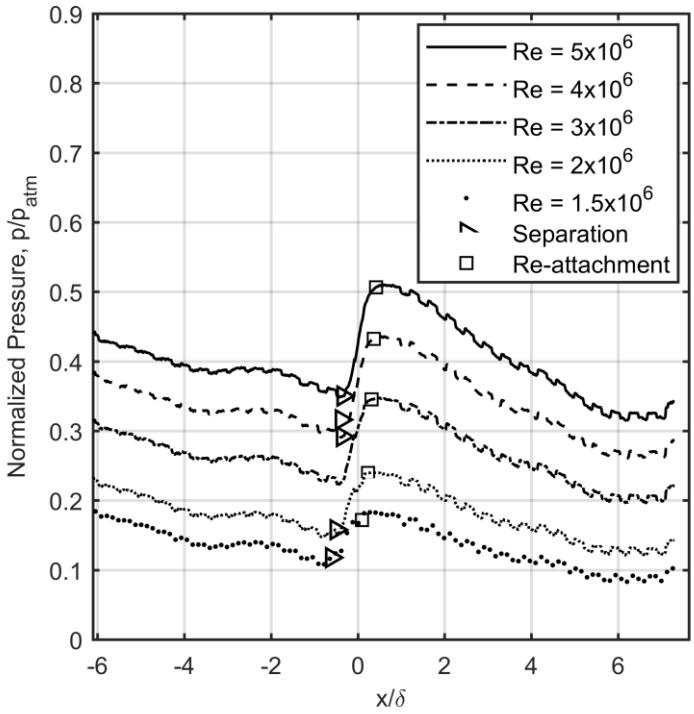

Figure 4. Normalized surface pressure profiles by the atmospheric pressure along the *x*-coordinate.

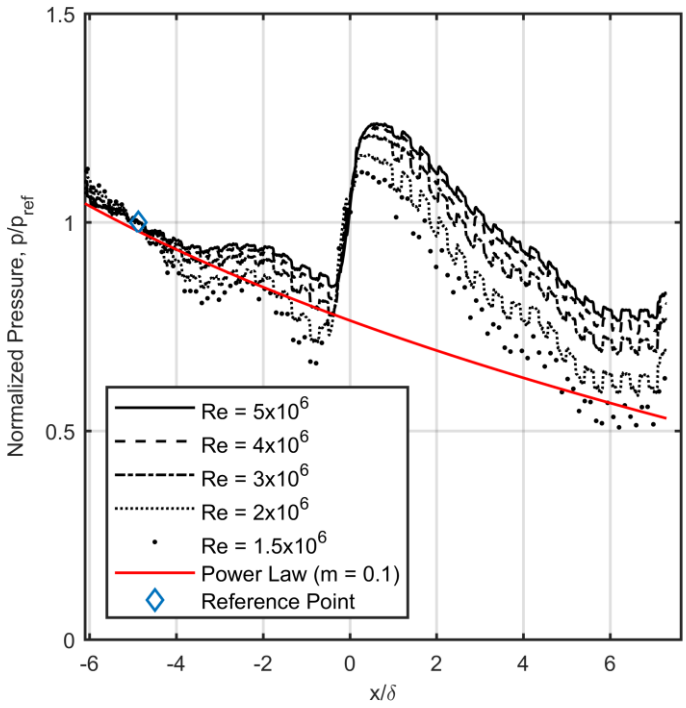

Figure 5. Surface pressure profiles re-normalized by the values at a reference location marked in the figure for different Reynolds numbers (Re_D), and a power-law fitting of data for the incoming boundary layer.

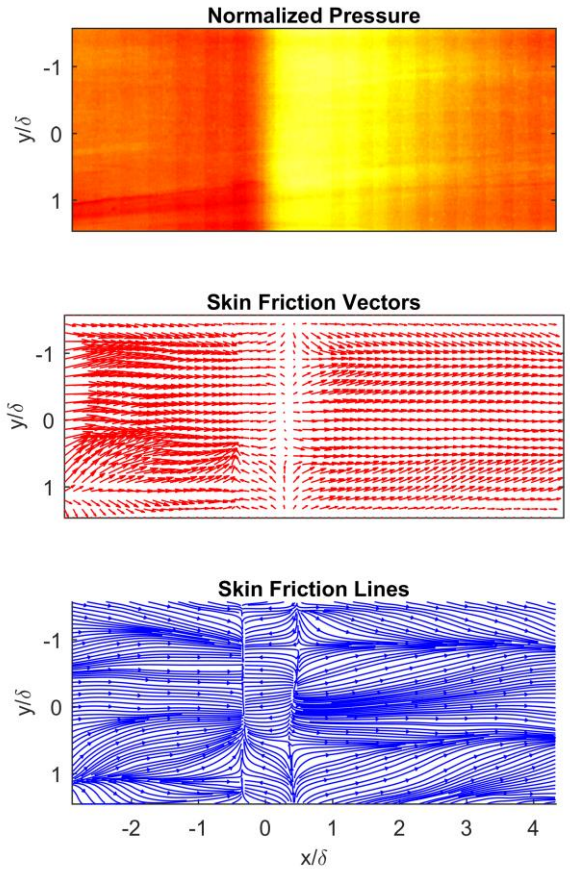

Figure 6. Time-averaged fields of the normalized surface pressure by its maximum value, extracted skin friction vectors and lines at Mach 2.5 for Re_D = 5 million. Flow is from left to right.

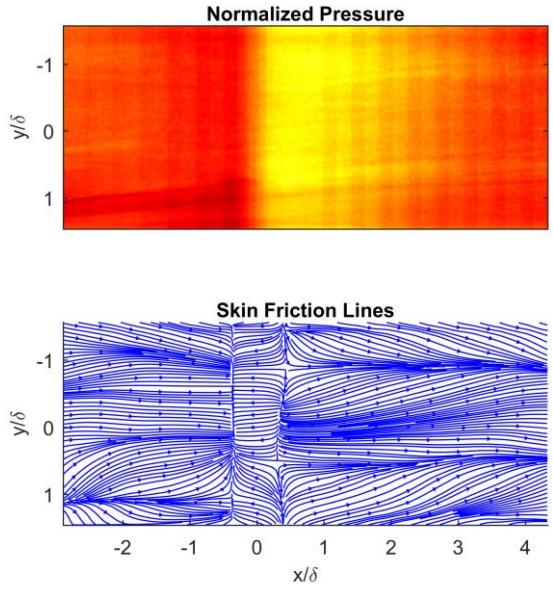

(a)

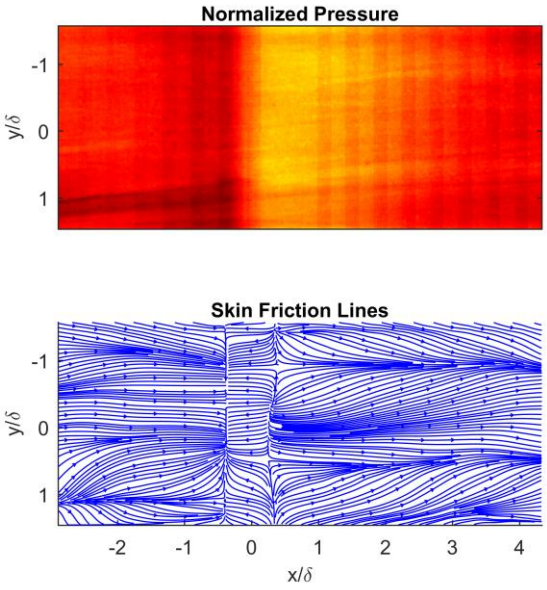

(b)

Figure 7 (Continued)

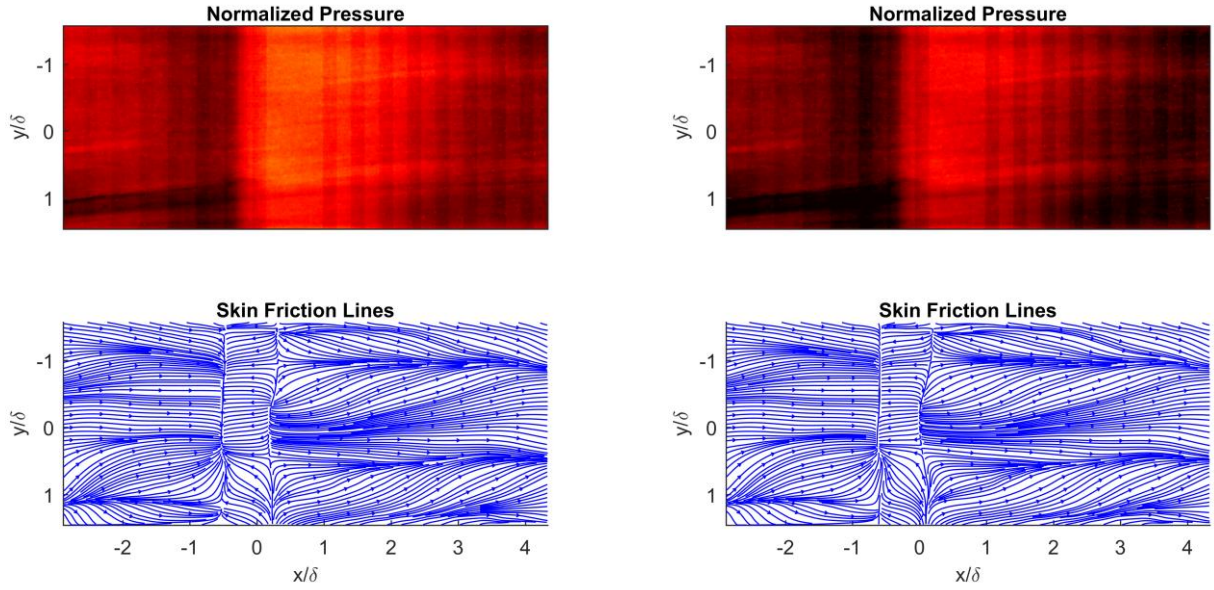

(c) (d)

Figure 7. Time-averaged fields of the normalized surface pressure by its maximum value and extracted skin friction lines at Mach 2.5 for Re_D = (a) 4, (b) 3, (c) 2, and (d) 1.5 million. Flow is from left to right.

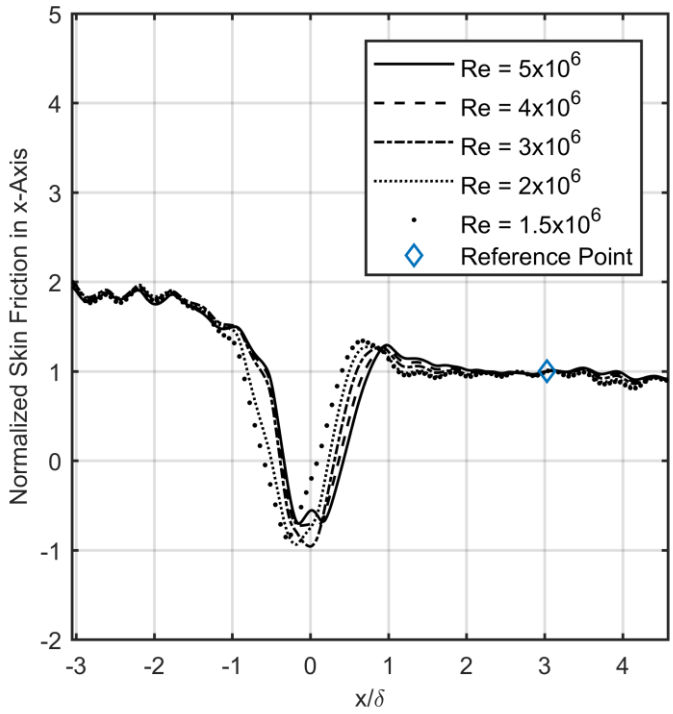

Figure 8. Profiles of the *x*-component of skin friction normalized by the values at a reference location marked in the figure at Mach 2.5 for different Reynolds numbers (Re_D).

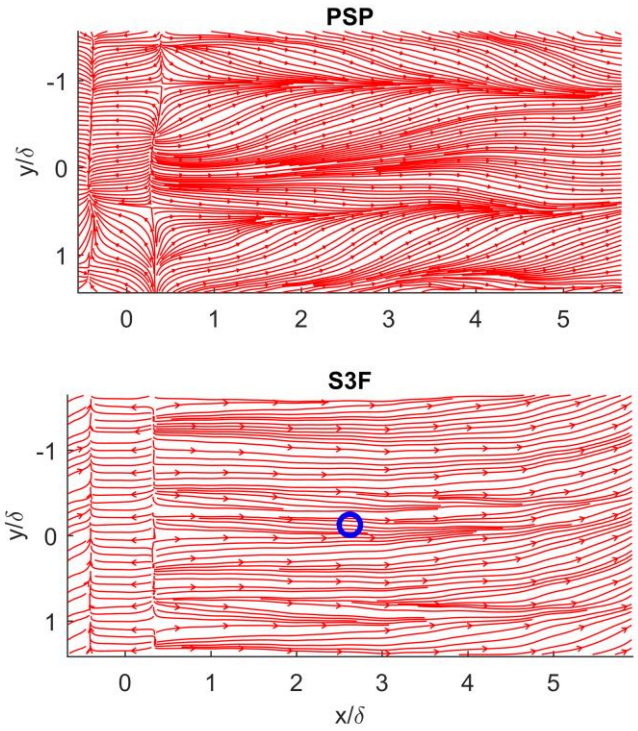

Figure 9. Comparison between skin friction lines obtained by PSP and S3F for Re_D = 2 million, where the circle marks the reference location for in-situ calibration. Flow is from left to right.

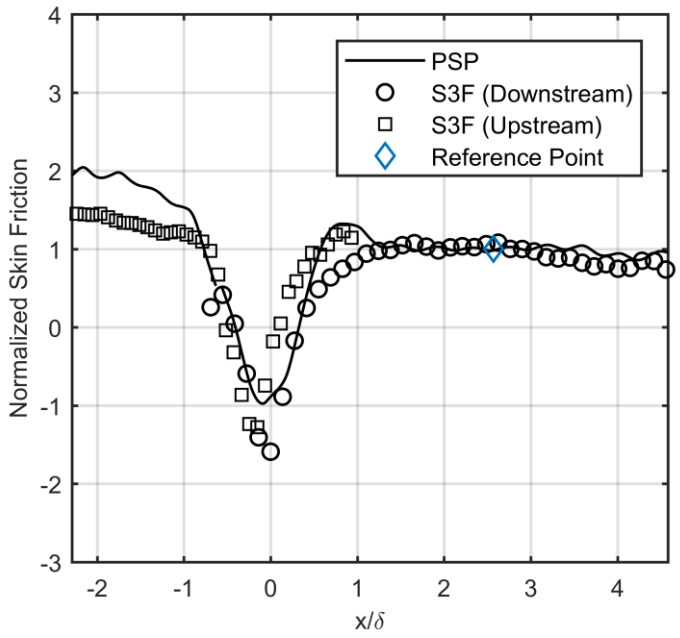

Figure 10. Comparison between profiles of the *x*-component of skin friction obtained by PSP and S3F for Re_D = 2 million, where the diamond marks the reference location for in-situ calibration.

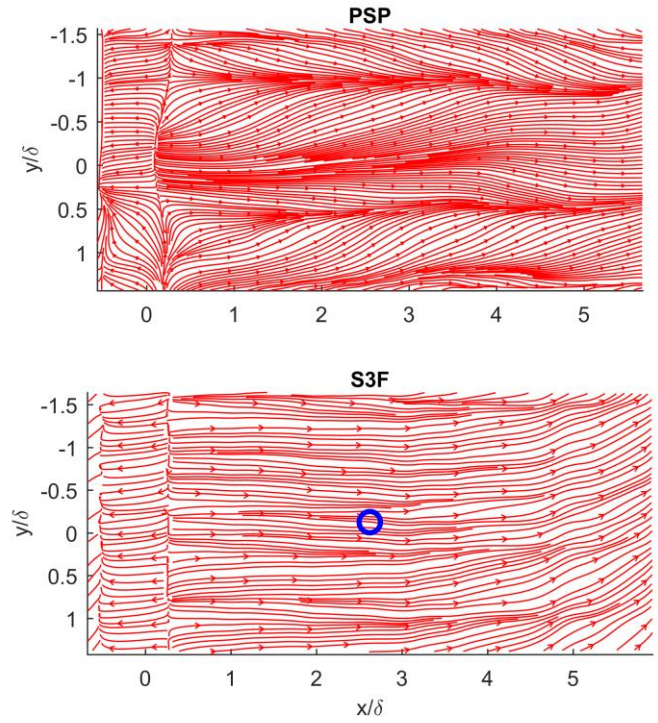

Figure 11. Comparison between skin friction lines obtained by PSP and S3F for Re_D = 1.5 million, where the circle marks the reference location for in-situ calibration. Flow is from left to right.

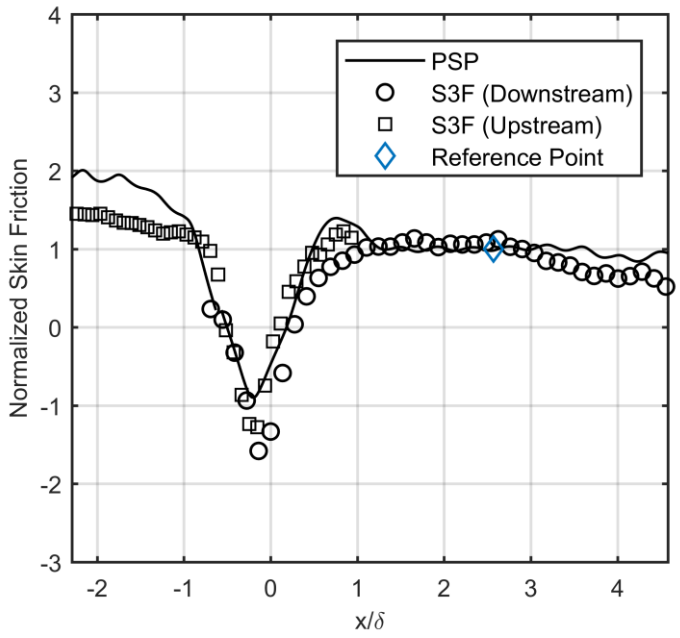

Figure 12. Comparison between profiles of the x-component of skin friction obtained by PSP and S3F for Re_D = 1.5 million, where the diamond marks the reference location for in-situ calibration.

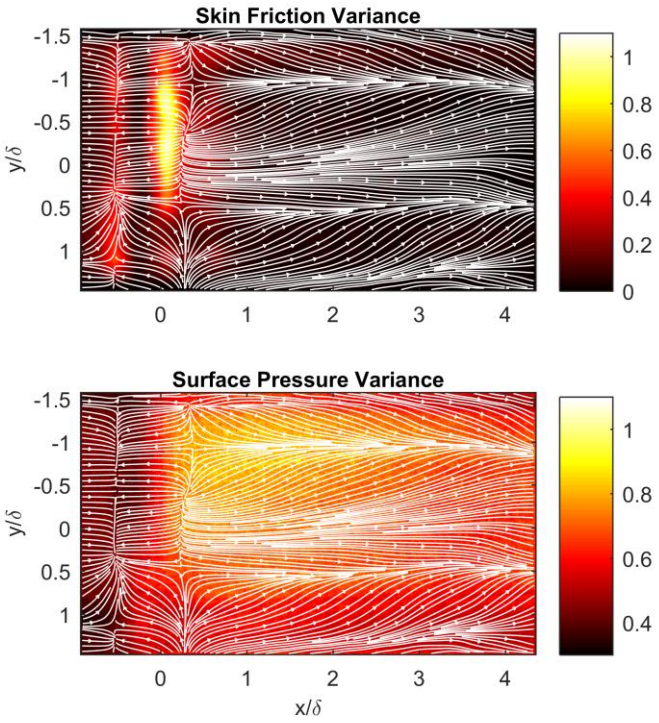

Figure 13. Fields of the normalized variances of surface pressure and skin friction fluctuations by the maximum values at Mach 2.5 for Re_D = 2 million. Flow is from left to right.

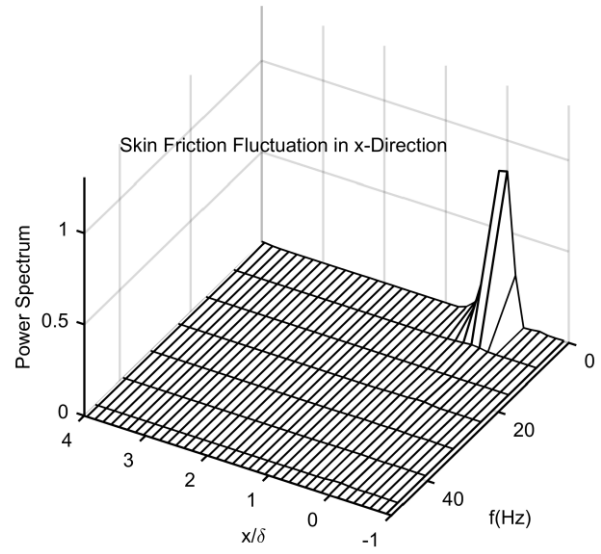

(a)

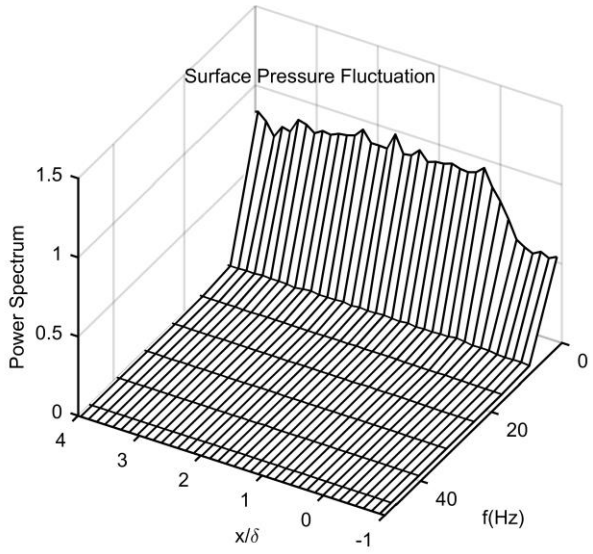

(c)

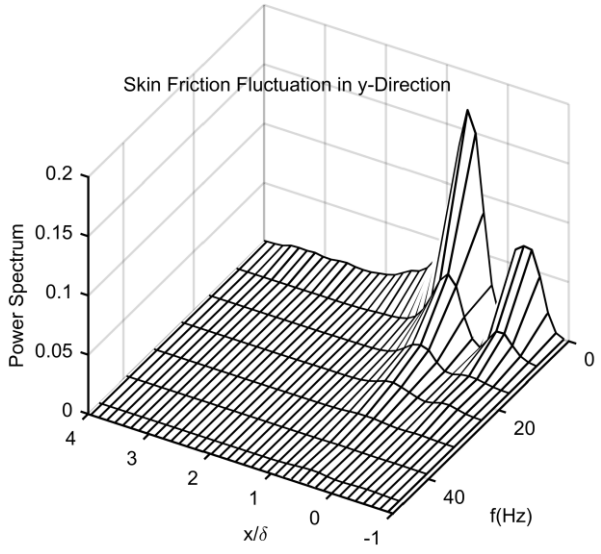

(b)

Figure 14. Energy spectra of skin friction and surface pressure fluctuations along the streamwise centerline of the measurement region at Mach 2.5 for Re_D = 2 million.

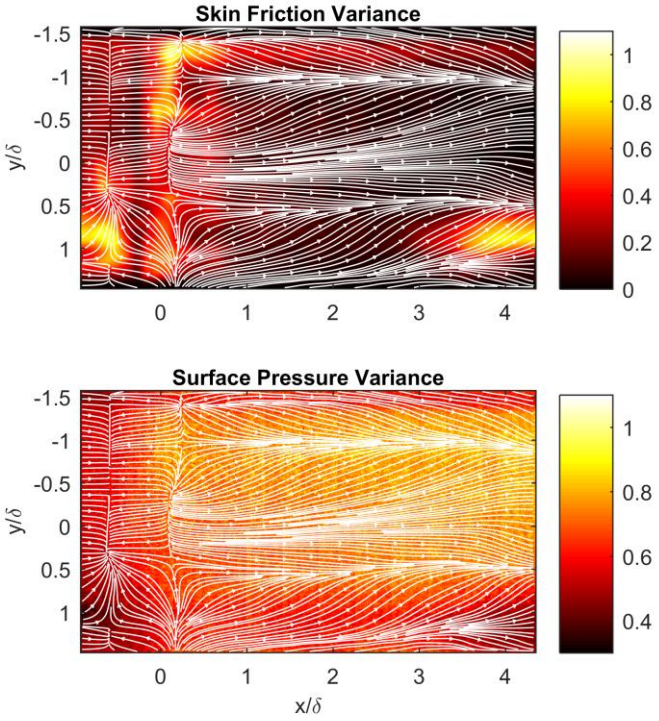

Figure 15. Fields of the normalized variances of surface pressure and skin friction fluctuations by the maximum values at Mach 2.5 for Re_D = 1.5 million. Flow is from left to right.

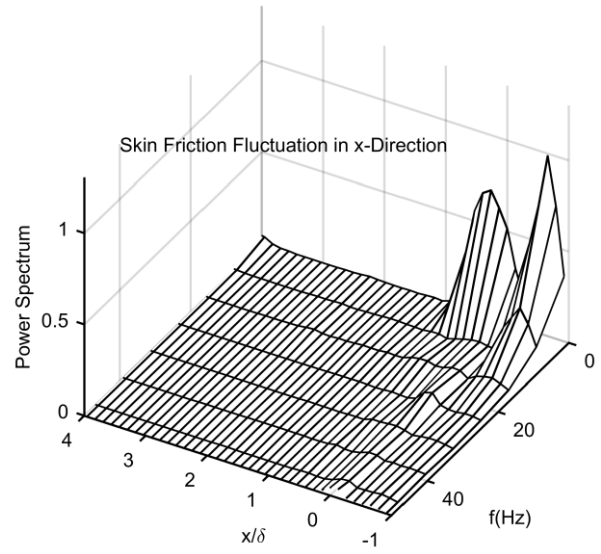

(a)

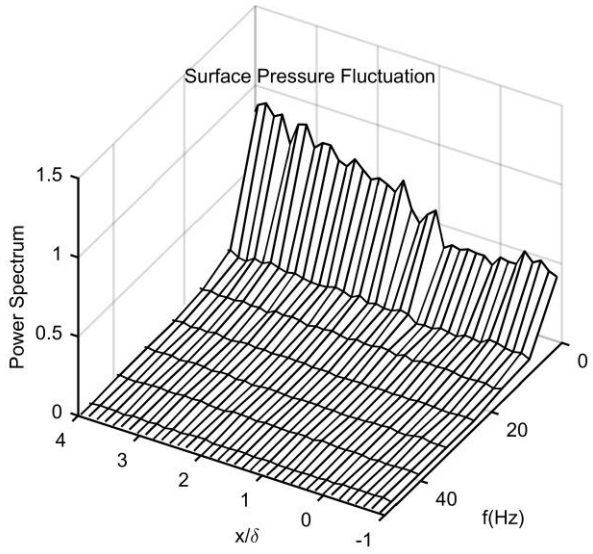

(c)

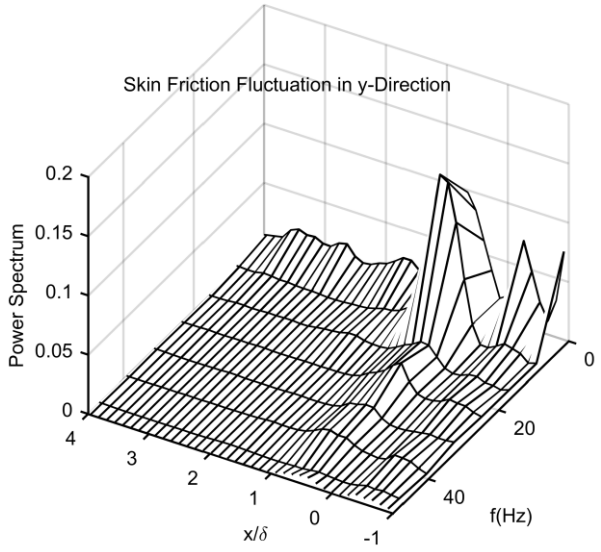

(b)

Figure 16. Energy spectra of skin friction and surface pressure fluctuations along the streamwise centerline of the measurement region at Mach 2.5 for Re_D = 1.5 million.

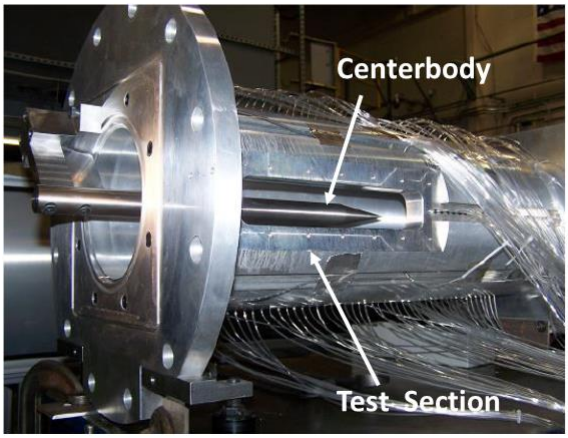

Figure A1. Mach 2.5 axisymmetric test section with a shock generator installed and window opening for optical techniques [38].

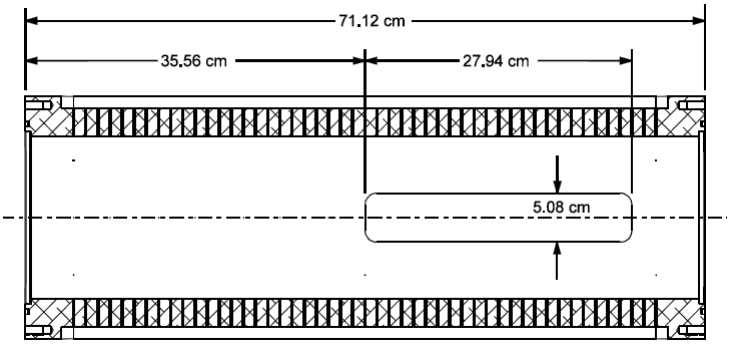

Figure A2. Schematic of the test section and window with the dimensions [38].

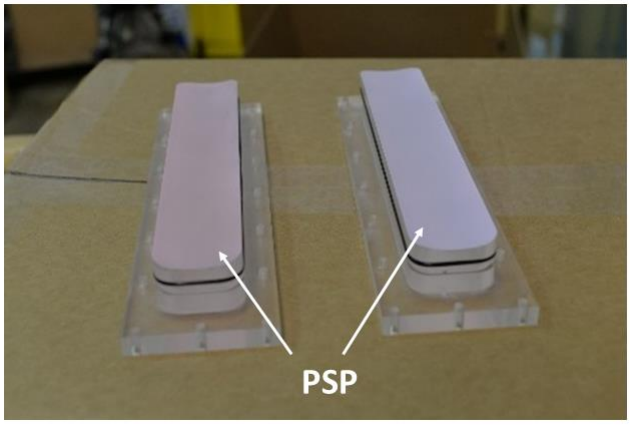

(a)

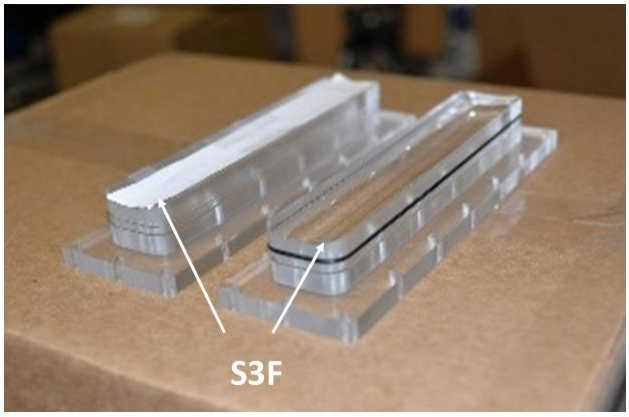

(b)

Figure A3. Test section windows with (a) PSP and (b) S3F applied [37].

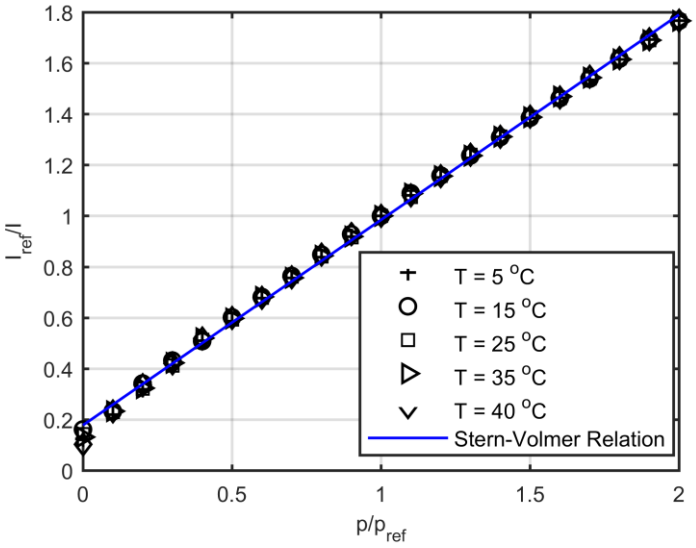

(a)

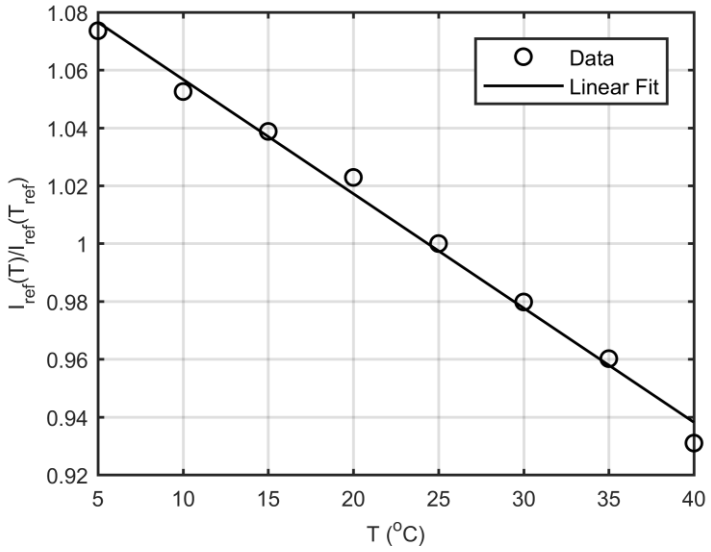

(b)

Figure A4. Calibration of ISSI Turbo PSP: (a) the Stern-Volmer plots, and (b) the reference intensity as a function temperature.

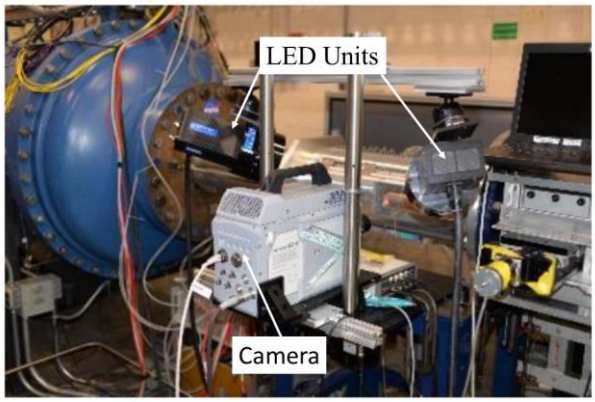

Figure A5. PSP measurement setup at the Mach 2.5 axisymmetric test section [37].

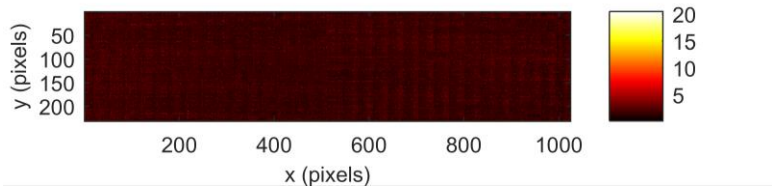

(a)

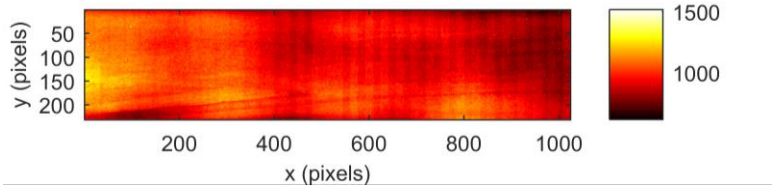

(b)

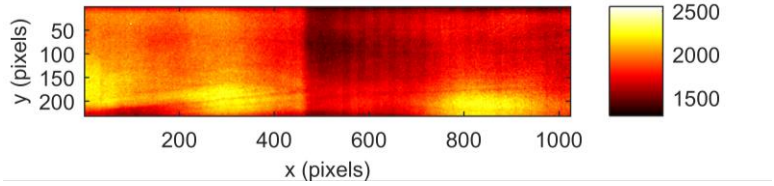

(c)

Figure B1. Raw images in Case 3466: (a) dark current image, (b) wind-off PSP image, and (c) wind-on PSP image. Flow is from left to right.